# Electronic Structural Flexibility of Heterobimetallic Mn/Fe Cofactors: R2lox and R2c Proteins

Hannah S. Shafaat,[†] Julia J. Griese,[‡] Dimitrios A. Pantazis,[†] Katarina Roos,[§] Charlotta S. Andersson,[‡] Ana Popović-Bijelić,[‡] Astrid Gräslund,[‡] Per E. M. Siegbahn,[§] Frank Neese,[†] Wolfgang Lubitz,[†] Martin Högbom,[‡] and Nicholas Cox*,[†]

[†]Max-Planck-Institut für Chemische Energiekonversion, Stiftstrasse 34-36, Mülheim an der Ruhr D-45470, Germany
[‡]Department of Biochemistry and Biophysics, Stockholm University, Stockholm SE-106 91, Sweden
[§]Department of Physics, Stockholm University, Stockholm SE-106 91, Sweden

**S** *Supporting Information*

**ABSTRACT:** The electronic structure of the Mn/Fe cofactor identified in a new class of oxidases (R2lox) described by Andersson and Högbom [*Proc. Natl. Acad. Sci. U.S.A.* **2009**, 106, 5633] is reported. The R2lox protein is homologous to the small subunit of class Ic ribonucleotide reductase (R2c) but has a completely different in vivo function. Using multifrequency EPR and related pulse techniques, it is shown that the cofactor of R2lox represents an antiferromagnetically coupled $Mn^{III}$/$Fe^{III}$ dimer linked by a $\mu$-hydroxo/bis-$\mu$-carboxylato bridging network. The $Mn^{III}$ ion is coordinated by a single water ligand. The R2lox cofactor is photoactive, converting into a second form (R2lox$_{Photo}$) upon visible illumination at cryogenic temperatures (77 K) that completely decays upon warming.



This second, unstable form of the cofactor more closely resembles the $Mn^{III}$/$Fe^{III}$ cofactor seen in R2c. It is shown that the two forms of the R2lox cofactor differ primarily in terms of the local site geometry and electronic state of the $Mn^{III}$ ion, as best evidenced by a reorientation of its unique $^{55}Mn$ hyperfine axis. Analysis of the metal hyperfine tensors in combination with density functional theory (DFT) calculations suggests that this change is triggered by deprotonation of the $\mu$-hydroxo bridge. These results have important consequences for the mixed-metal R2c cofactor and the divergent chemistry R2lox and R2c perform.
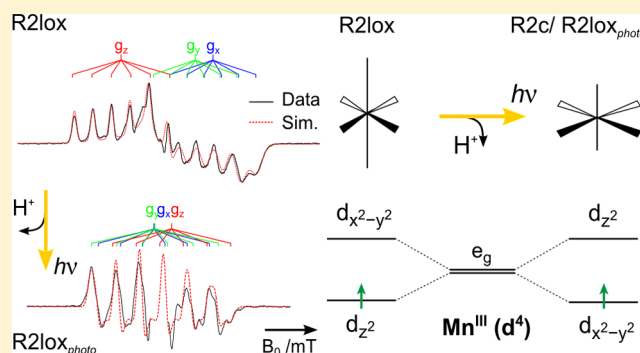
## 1. INTRODUCTION

Heterobimetallic cofactors are found in an increasing number of proteins and perform a diverse range of chemical reactions. Examples include the Ni/Fe cofactor of the [NiFe]-hydrogenase, which produces and oxidizes hydrogen,[1] the heme a3/CuB arrangement in cytochrome *c* oxidase, which reduces dioxygen,[2] and the Cu/Zn binding motif of eukaryotic SOD, which detoxifies (dismutates) the superoxide radical.[3] Recently, this set has been extended to Mn/Fe-containing proteins, which are activated by molecular oxygen. The Mn/Fe cofactor was first identified in a variant of purple acid phosphatase[4] and has subsequently been proposed as the native cofactor of the small subunit (R2) of class I ribonucleotide reductase (RNR) from *Chlamydia trachomatis* (*Ct*R2c)[5,6] and possibly an N-oxygenase from yeast.[7−9]

The R2 subunit of class I RNR acts as a single-electron oxidant, initiating catalytic conversion of ribonucleotides to deoxyribonucleotides.[10−12] In most subclasses of R2, the one-electron oxidant is stored in the form of a tyrosyl radical in close proximity to a dinuclear metal cofactor (Fe/Fe in class Ia[13−15] or Mn/Mn in class Ib[16−18]). It is the metallocofactor

that initially oxidizes the tyrosine via its reaction with oxygen or a reactive oxygen species (ROS).[19] However, the R2 subclass that contains a Mn/Fe cofactor (R2 class Ic, R2c) adopts a different strategy. While the active catalytic site is also generated via oxygen activation, the redox-active tyrosine residue is replaced by a redox-inert phenylalanine[20] and the oxidizing equivalent is instead stored at the metal cofactor itself in the form of the high-valent $Mn^{IV}$/$Fe^{III}$ state.[5,6] A crystal structure of the activated, mixed-metalated R2c with full occupancy has yet to be reported. However, a structure of the presumably nonphysiological di-iron cofactor in *Ct*R2c has been determined in the resting ($Fe^{III}$/$Fe^{III}$) state,[20] and more recently, a structure of the preactivated $Mn^{II}$/$Fe^{II}$ state was reported (Figure 1A and 1B).[21] It is unclear to what extent the activated Mn/Fe cofactor differs from the activated di-iron state.

A homologous Mn/Fe cofactor to that seen in R2c was recently discovered and structurally characterized in two R2-
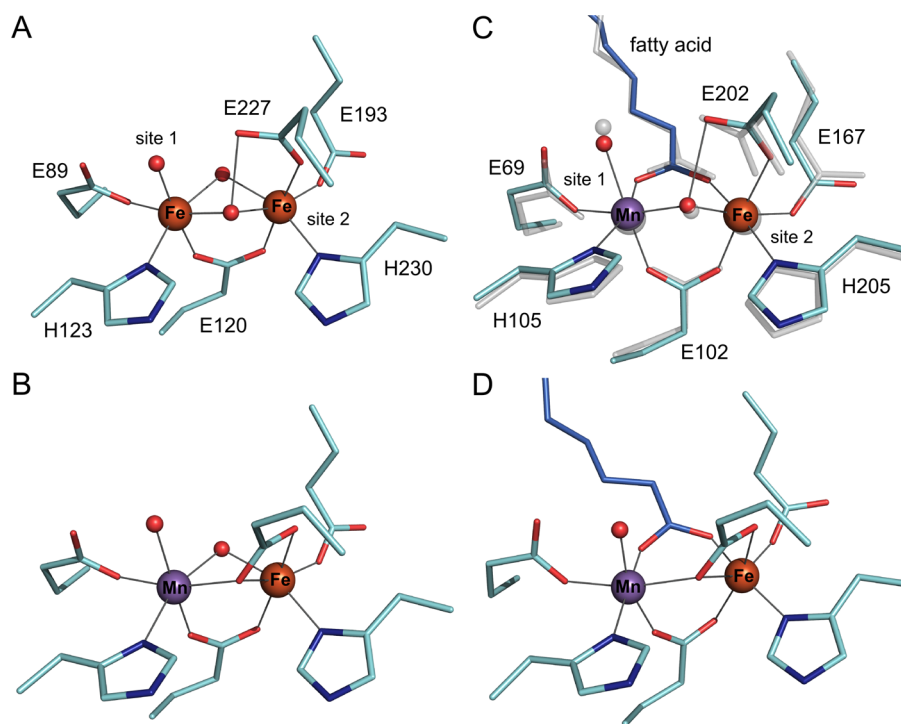
**Figure 1.** Crystal structures of R2c and R2lox proteins. (A) The oxidized Fe/Fe-cofactor of *Ct*R2c (PDB ID 1SYY)[20] at 1.7 Å resolution. (B) The reduced Mn/Fe cofactor of *Ct*R2c (PDB ID 4M1I)[21] at 1.8 Å resolution. (C) Superposition of the oxidized Mn/Fe-bound active sites of *Gk*R2loxI (cyan, metal-coordinating residues; blue, fatty acid ligand; PDB ID 4HR0)[23] and *Mt*R2lox (gray; PDB ID 3EE4),[22] both at 1.9 Å resolution. Residue numbering is for *Gk*R2loxI. (D) The reduced Mn/Fe-bound active site of *Gk*R2loxI (PDB ID 4HR4)[23] at 1.9 Å resolution.

like proteins from the pathogenic bacterium *Mycobacterium tuberculosis* (Rv0233, *Mt*R2lox)[22] and the thermophilic bacterium *Geobacillus kaustophilus* (*Gk*R2loxI)[23] (Figure 1C and 1D). Owing to the structural similarity this new class of proteins has with R2c, they are referred to as "R2lox", as in ribonucleotide reductase R2-like ligand-binding oxidase. Although an in vivo function for the R2lox protein has yet to be identified, it is anticipated that the chemistry it performs resembles that of the Mn/Fe cofactor of R2c, i.e., that the cofactor acts as an oxidant. Under anaerobic conditions, the protein is inactive, binding metals in the +II oxidation state. In the presence of oxygen, an oxo/hydroxo bridged cofactor is formed with the concomitant two-electron oxidation of a nearby protein side chain, generating a covalent ether cross-link between a tyrosine and a normally inert valine residue.[22,23]

Both R2lox proteins were isolated and crystallized with an exogenous lipid bound, and in both cases the carboxylate headgroup provided an oxygen ligand to each of the metal sites (Figure 1C and 1D).[22,23] As a consequence, it has been speculated that its biological function is that of a lipid oxidase or possibly a desaturase.[22−24] Both in R2c and in R2lox, the Mn/Fe cofactor is assembled with the Mn ion located in site 1.[21−23,25,26] Structurally, the two cofactors appear to be almost identical, with the only difference being the fatty acid ligand in R2lox which takes the place of an oxo/hydroxo bridge in R2c (Figure 1). It is unclear therefore how the Mn/Fe cofactor is directed toward 1e⁻ redox chemistry in R2c vs 2e⁻ redox chemistry in R2lox.

Because of the complexity of large metalloprotein systems, site-specific spectroscopies such as electron paramagnetic resonance (EPR) are invaluable tools, providing details on the structure of the metal site. EPR results complement those obtained with X-ray crystallography as the protein can be

measured under dilute conditions in a near-native, solvated environment, representing the active, unperturbed conformation. Furthermore, because high-valent, oxidized Mn and Fe cofactors are highly susceptible to photoreduction during X-ray data collection,[27−30] EPR has the added advantage of being a nondestructive technique. In terms of manganese metallocofactors, EPR studies have provided direct information on the oxidation state of the metal ion(s)[16,31,32] and the identity and protonation state of first coordination sphere ligands (for recent examples see refs 33−35). In systems performing multielectron catalysis, EPR can also be used to monitor the cofactor reaction cycle, providing information on structural rearrangements, substrate binding, and reactivity.

In this work, a complete description of the electronic structure of the R2lox metallocofactor is assessed using a comprehensive set of EPR techniques, including CW and pulse experiments at X-, Q-, and W-band frequencies in conjunction with ENDOR and ESEEM methods[34,36,37] to probe nuclear transitions coupled to the active site. It is shown that the oxidized, Mn$^{III}$/Fe$^{III}$ cofactor is similar to synthetic Mn$^{III}$/Fe$^{III}$ and isoelectronic Mn$^{II}$/Mn$^{III}$ complexes such as those reported by Wieghardt and co-workers.[38,39] The discrete metalation of each site could be assessed via the first coordination sphere ligands (¹⁴N-histidine), which serve as local spin reporters on metal identity. This novel technique allows a semiquantitative assessment of mismetalation in heterobimetallic cofactors, with broad applicability. The oxidation state, electronic structure, and ligand arrangement of the cofactor are discussed in the context of site selectivity, cofactor assembly, and its in vivo activity as compared to R2c.

## 2. EXPERIMENTAL SECTION

**2.1. EPR Sample Preparation.** The R2lox protein from *Mycobacterium tuberculosis* (Rv0233, *Mt*R2lox) was prepared in the oxidized Mn/Fe-bound state as described previously by Andersson and Högbom.[22] The R2lox protein homologue I from the thermophilic bacterium *Geobacillus kaustophilus* (accession number yp_148624, *Gk*R2loxI)[23] was used for most CW and all pulse EPR measurements. The *Gk*R2loxI apoprotein was produced and purified as previously described by Griese et al.[23] Protein concentrations were determined using an extinction coefficient at 280 nm of 47.76 and 50.56 mM$^{-1}$ cm$^{-1}$ for metal-free and metal-bound *Gk*R2loxI, respectively. These extinction coefficients were obtained by measuring the absorbance at 280 nm of metal-free and metal-bound protein before and after unfolding with 5.4 M guanidine hydrochloride and using the calculated extinction coefficient at 280 nm for the unfolded *Gk*R2loxI monomer of 45.87 mM$^{-1}$ cm$^{-1}$. To reconstitute the oxidized Mn/Fe cofactor, 200 $\mu$M apoprotein was incubated with 2 equiv of MnCl$_2$ and 1 or 2 equiv of (NH$_4$)$_2$Fe(SO$_4$)$_2$ in 100 mM HEPES-Na pH 7.0, 50 mM NaCl for 1 h at room temperature. Excess metal ions were removed by passing the sample through a HiTrap Desalting column (GE Healthcare) equilibrated in 25 mM HEPES-Na pH 7.0, 50 mM NaCl. The reconstituted protein was concentrated to 0.4−1.4 mM, and 50% glycerol was added before transfer into X-, Q-, and W-band EPR tubes and flash freezing in liquid nitrogen. To label the oxidized cofactor with $^{57}$Fe, $^{57}$FeSO$_4$ was used instead of natural abundance (NH$_4$)$_2$Fe(SO$_4$)$_2$. Mn$^{III}$/Fe$^{III}$-reconstituted samples were exchanged into $^2$H$_2$O-based buffer (25 mM HEPES-Na pD 7.0, 50 mM NaCl) by four rounds of dilution and concentration. Photo-excitation of the Mn$^{III}$/Fe$^{III}$ sample was carried out using a broad-band halogen lamp (12 V, 50 W) through a UV filter at 77 K.

**2.2. Multifrequency EPR Measurements.** X-Band EPR measurements were performed at 5−20 K using a Bruker E50 spectrometer, equipped with an Oxford Instruments ESR 935 cryostat and ITC4 temperature controller. X and Q-Band pulse EPR measurements were performed at 5 K using a Bruker ELEXSYS2 E580 (X-band) and a Bruker ELEXSYS E580 (Q-band) pulse EPR spectrometer, equipped with a home-built TE$_{011}$ microwave cavity (Q-band),[40] Oxford-CF935 liquid helium cryostat, and an ITC-503 temperature controller. High-field EPR experiments were performed at 4.8 K using a W-band EPR spectrometer (Bruker ELEXSYS E680) operating at about 94 GHz, as described in Rapatskiy et al.[34] Free induction decay detected (FID) field-swept spectra were measured using pulse lengths of: 2000 ns (X-band) and 1000 ns (Q-band). Electron spin echo-detected (ESE) field-swept spectra were measured using the pulse sequence: $t_p-\tau-2t_p-\tau-$echo. The length of the $\pi/2$ microwave pulse was generally set to $t_p =$ 8 (X-band), 12 (Q-band), and 24 ns (W-band). The interpulse distance was varied in the range $\tau = 140-200$ (X-band), 200−500 ns (Q-band) and $\tau = 248-500$ ns (W-band). Pseudomodulated EPR spectra were generated by convoluting the original absorption spectra with a Bessel function of the first kind. The peak-to-peak amplitude used was 2−3 mT. Three pulse X and Q/W-band $^{14}$N-ESEEM spectra were measured using the pulse sequence $t_p-\tau-t_p-T-t_p-\tau-$echo. The same pulse length as for the ESE spectra were used. The interpulse distance ($\tau$) was set to $\tau = 196$ ns (X-band) and $\tau = 236$ ns (Q/W-band) The interpulse distance $T$ was sampled in the range of 100−16500 (X-band) and 100−4100 ns (Q/W-band). The time base increment ($\Delta T$) was 32 (X-band) and 8 ns (Q/W-band). Q-Band $^2$H-HYSCORE spectra were measured using the pulse sequence $t_p-\tau-t_p-t_1-2t_p-t_2-t_p-\tau-$echo. A pulse length of $t_p = 12$ ns and interpulse spacing of $\tau = 240$ ns were used. The interpulse distances $t_1$ and $t_2$ were sampled in the range of 100−2000 ns. The time base increment ($\Delta t_1, \Delta t_2$) was 32 ns. A shot repetition rate of ~1−2 kHz was typically used for EPR measurements. Q-Band Davies $^{55}$Mn-ENDOR and $^1$H-ENDOR spectra were collected using the pulse sequence $t_{inv}-t_{RF}-T-t_p-\tau-2t_p-\tau-$echo using an inversion microwave pulse length of $t_{inv} = 24$ ($^{55}$Mn) and 128 ns ($^1$H) and a radiofrequency pulse length of $t_{RF} = 3.5$ ($^{55}$Mn) and 20 $\mu$s ($^1$H). The length of the $\pi/2$ microwave pulse in the detection sequence was generally set to $t_p = 12$ ($^{55}$Mn) and 64 ns ($^1$H) and the interpulse delays to $T = 0.6$ ($^{55}$Mn) and 1.5 $\mu$s ($^1$H) and

$\tau = 396-468$ ns. The RF frequency was swept between 80 and 200 MHz in 500 kHz steps to collect $^{55}$Mn-ENDOR spectra and 20 MHz around the $^1$H-Larmor frequency of about 52 MHz (1.2 T) in 100 kHz steps to collect $^1$H-ENDOR spectra. A larger sweep of 80−320 MHz in 750 kHz steps was used to collect 55Mn-ENDOR spectra of the R2lox$_{Photo}$ state.

**2.3. EPR Spin Hamiltonian Simulations.** Spectra were simultaneously fitted assuming the two metals antiferromagnetically coupled to yield an effective spin $S = 1/2$ ground state (for details see Supporting Information). The basis set that describes the interaction of the unpaired electron with the metal nuclei ($^{55}$Mn, $^{57}$Fe) and its interaction with magnetic nuclei of the first coordination sphere ligands can be built from the product of the eigenstates of the interacting spins

$$\left| \frac{1}{2} M I_1 m_1 I_2 m_2 I_3 m_3 \right\rangle$$

$I_1$ takes the value 5/2 for $^{55}$Mn, $I_2$ takes the value 1/2 for $^{57}$Fe, and $I_3$ takes the value 1 for $^2$H/$^{14}$N and 1/2 for $^1$H/$^{57}$Fe. $M_i$ refers to the electronic magnetic sublevel and takes the values $\pm 1/2$; $m_i$ refers to the nuclear magnetic sublevel and takes the values $-I_i, 1 - I_i, ..., I_i - 1, I_i$. As the magnetic interactions of the ligand nuclei with the electron spin are small, these interactions do not contribute to the inhomogeneous line width of the metallocofactor's EPR spectrum. Similarly, nuclear−nuclear interactions are negligible in magnitude relative to the electron−nuclear interaction, allowing each ligand−electron interaction to be treated independently.

The spin Hamiltonian that describes the spin manifold is

$$\hat{H}_{Tot} = \hat{H}_{electron} + \hat{H}_{metal} + \hat{H}_{ligand}$$

where the three components are

$$\hat{H}_{electron} = \beta_e \vec{B}_0 \cdot \hat{g} \cdot \vec{S}$$

$$\hat{H}_{metal} = -g_{Mn}\beta_n \vec{B}_0 \cdot \vec{I}_1 + \vec{S} \cdot \hat{A}_1 \cdot \vec{I}_1 + \vec{I}_1 \cdot \hat{Q}_1 \cdot \vec{I}_1$$
$$ - g_{Fe}\beta_n \vec{B}_0 \cdot \vec{I}_2 + \vec{S} \cdot \hat{A}_2 \cdot \vec{I}_2 + \vec{I}_2 \cdot \hat{Q}_2 \cdot \vec{I}_2$$

$$\hat{H}_{ligand} = -g_L \beta_n \vec{B}_0 \cdot \vec{I}_3 + \vec{S} \cdot \hat{A}_3 \cdot \vec{I}_3 + \vec{I}_3 \cdot \hat{Q}_3 \cdot \vec{I}_3$$

It contains (i) the Zeeman term for the total electron spin, (ii) the Zeeman term for the nucleus, (iii) the hyperfine term for the nucleus, and (iv) the quadrupole term for the nucleus. Spectral simulations were performed numerically using the EasySpin package[41,42] in MATLAB (Mathworks Inc., Natick, MA).

**2.4. Density Functional Theory (DFT) Calculations.** Model geometries were taken from Griese et al.[23] and used as published. Exchange coupling constants, hyperfine tensors, and nuclear quadrupole tensors were computed using the broken-symmetry density functional theory (BS-DFT) approach.[43−46] All calculations were performed with ORCA.[47] The hybrid meta-GGA TPSSh functional[48] was used because it has been extensively calibrated in recent studies of magnetic and spectroscopic parameters of manganese systems.[39,49−53] Scalar relativistic effects were included with the zero-order regular approximation (ZORA).[54−56] The resolution of the identity (RI) and the chain of spheres approximation (COSX)[45] were used for the Coulomb and exact exchange, respectively. The ZORA-contracted def2-TZVP(-f) SARC basis sets[57] were employed for all atoms, combined with fully decontracted def2-TZVP/J auxiliary basis sets.[58] Tight SCF convergence and increased integration grids (Grid6 and GridX6 in ORCA notation) were applied. For calculation of the hyperfine and quadrupole tensors, basis sets with added flexibility in the core region were used for the metal and ligand atoms. These basis sets are based on SARC ZORA-def2-TZVP but have fully decontracted s shells with three additional functions obtained by multiplying the exponent of the steepest original primitive with 2.5, 6.25, and 15.625. As previously described,[39] this follows the procedure introduced in ref 59 with the added benefit that the higher angular momentum subspaces are consistently contracted[57] for the ZORA Hamiltonian. Picture change effects (the effect of using appropriate

quasi-relativistic property operators for the quasi-relativistic wave function) were applied for calculation of EPR parameters, and the complete mean-field approach was used for the spin−orbit coupling operator. Radial integration grids were increased to an integration accuracy of 12 and 9 (ORCA convention) for the metal and ligand atoms, respectively.

## 3. RESULTS AND DISCUSSION

**3.1. R2lox Contains a Mn$^{III}$/Fe$^{III}$ Cofactor.** A preliminary description of the electronic structure of the aerobically reconstituted cofactor of R2lox was recently provided in Griese et al.[23] Its frozen solution CW X-band EPR spectrum is characteristic of a heterobimetallic Mn$^{III}$/Fe$^{III}$ cofactor as shown in Figure 2A and 2B and is essentially the same for
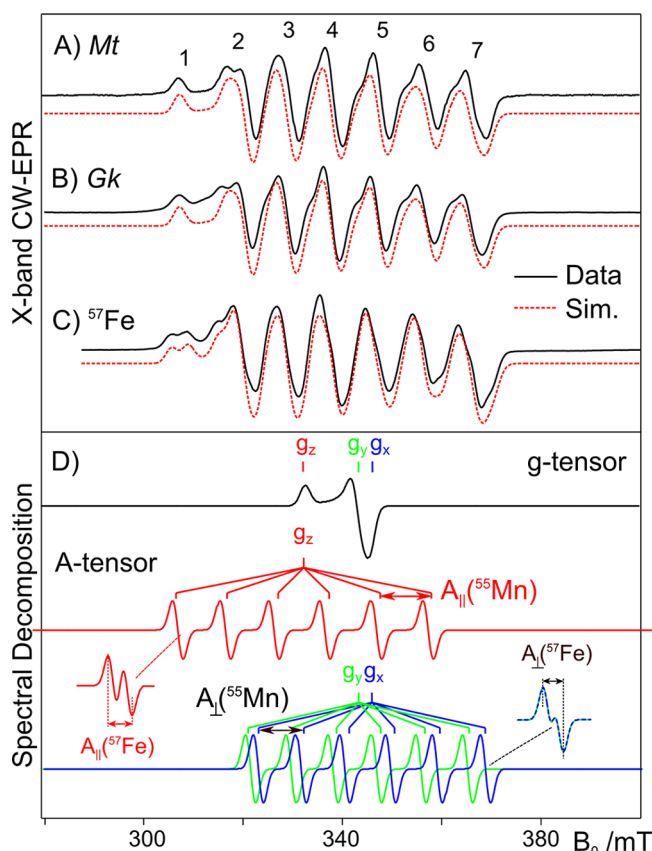


**Figure 2.** CW X-band (9.47 GHz) EPR spectra (black lines) and spin Hamiltonian simulations (red dashed lines) of the R2lox cofactor. (A) The Mn/Fe metallocofactor observed in *Mt*R2lox showing its characteristic seven line structure; (B) the homologous metallocofactor seen in *Gk*R2loxI;[23] (C) the *Gk*R2loxI metallocofactor labeled with $^{57}$Fe;[23] (D) a decomposition of the spin Hamiltonian simulation. The top black trace shows the inferred g-tensor of the metallocofactor. The lower colored traces show the hyperfine structure that superimposes the g-tensor. The sum of the hyperfine patterns results in the observed seven-line structure. Simulation parameters are given in Table 1.

both R2lox proteins isolated to date, *Mt*R2lox[22] and *Gk*R2loxI.[23] The metallocofactor X-band spectrum displays a characteristic seven-line structure (Figure 2A and 2B). This discrete line splitting obscures additional spectral information including resolution of the g-tensor, which describes the asymmetry and anisotropy of the unpaired electron(s)' chemical environment (Figure 2D). The EPR signal is consistent with the Fe$^{III}$ and Mn$^{III}$ ions ($S_1$, $S_2$) antiferromag-

netically coupled to yield an $S_T$ = 1/2 spin state.[23] The spectrum can be considered the superposition of two six-line patterns, derived from the hyperfine interaction of the unpaired electron spin and the $^{55}$Mn nucleus (natural abundance 100%) of the metallocofactor ($I(^{55}$Mn) = 5/2). An additional hyperfine structure due to the Fe nucleus can also be observed when reconstituting the cofactor using an $^{57}$Fe salt (Figure 2C). To best visualize the effects of g-value anisotropy and hyperfine interactions, a decomposition of the simulation is shown in Figure 2D. The powder EPR spectrum of the cofactor in the absence of the hyperfine interaction is shown by the black trace, resolving the three turning points (g-values) describing the three unique orientations of the molecular frame, which define the limits of the ensemble (powder) spectrum. Each of these g positions is split due to the hyperfine interaction into six evenly spaced lines. This decomposition demonstrates that the metallocofactor has approximately axial symmetry; there is one unique molecular axis with the other two appearing more similar, in terms of both the g-value (pattern position) and the metal ($^{55}$Mn, $^{57}$Fe) hyperfine splittings (peak spacing). The chemical significance of tensor axiality and colinearity forms the basis of our current study.

**3.2. Multifrequency EPR Measurements of the Mn/Fe Cofactor of R2lox.** Pulse EPR measurements were performed at multiple microwave frequencies (X-, Q-, and W-band) to complement the CW EPR measurements (Figure 3). Magnetic field swept spectra were collected using the standard two-pulse (echo) detection sequence and by free-induction decay (FID). Upon moving to higher microwave frequencies, the metallocofactor spectrum becomes more resolved, allowing the Zeeman and hyperfine interactions to be accurately determined. Indeed, the predictable frequency/field dependence of the metallocofactor spectrum suggests that it represents only one EPR species. Simulations using the spin Hamiltonian formalism (Figure 3 (red dashed lines)) reproduce all spectral features observed in the EPR data sets (see Supporting Information S1).

$^{55}$Mn-ENDOR was used to further characterize the Mn$^{III}$ ion of the active site (Figure 4a). ENDOR directly reports on the local properties of metal ions in spin exchange-coupled systems.[31,32] In these experiments, the hyperfine splitting seen in the EPR spectrum is measured directly via radio-frequency irradiation. The $^{55}$Mn-ENDOR spectrum essentially consists of a doublet centered about one-half the $^{55}$Mn hyperfine coupling interaction, split by twice the nuclear Larmor frequency [$\nu(^{55}$Mn) = 12.9 MHz at 1.22 T]. $^{55}$Mn-ENDOR signals are observed between 110 and 160 MHz, centered at ∼130 MHz, yielding a hyperfine coupling of 260 MHz (∼10 mT), consistent with the EPR data (Figure 4A). Importantly, the magnetic field dependence of the $^{55}$Mn-ENDOR data set constrains the orientations of both the $^{55}$Mn hyperfine and the quadrupole tensor relative to the molecular (g axis) frame, resolving the local electronic structure of the Mn ion (see section 3.4).

**3.3. Photoinduced State.** The absorption spectrum of *Gk*R2loxI shows a shoulder in the wavelength region 300−400 nm ($\varepsilon_{350} \approx 3000$ M$^{-1}$ cm$^{-1}$) trailing into the visible region that likely represents a ligand-to-metal charge transfer transition (Supporting Information S2).[60,61] Interestingly, photoexcitation into this transition using broad-band visible light at cryogenic temperatures leads to the loss of the Mn$^{III}$/Fe$^{III}$ cofactor signal described and emergence of a new EPR signal (Figure 5). This new species, denoted R2lox$_{Photo}$, is stable as long as the sample remains frozen (Supporting Information

13402

dx.doi.org/10.1021/ja507435t | *J. Am. Chem. Soc.* 2014, 136, 13399−13409
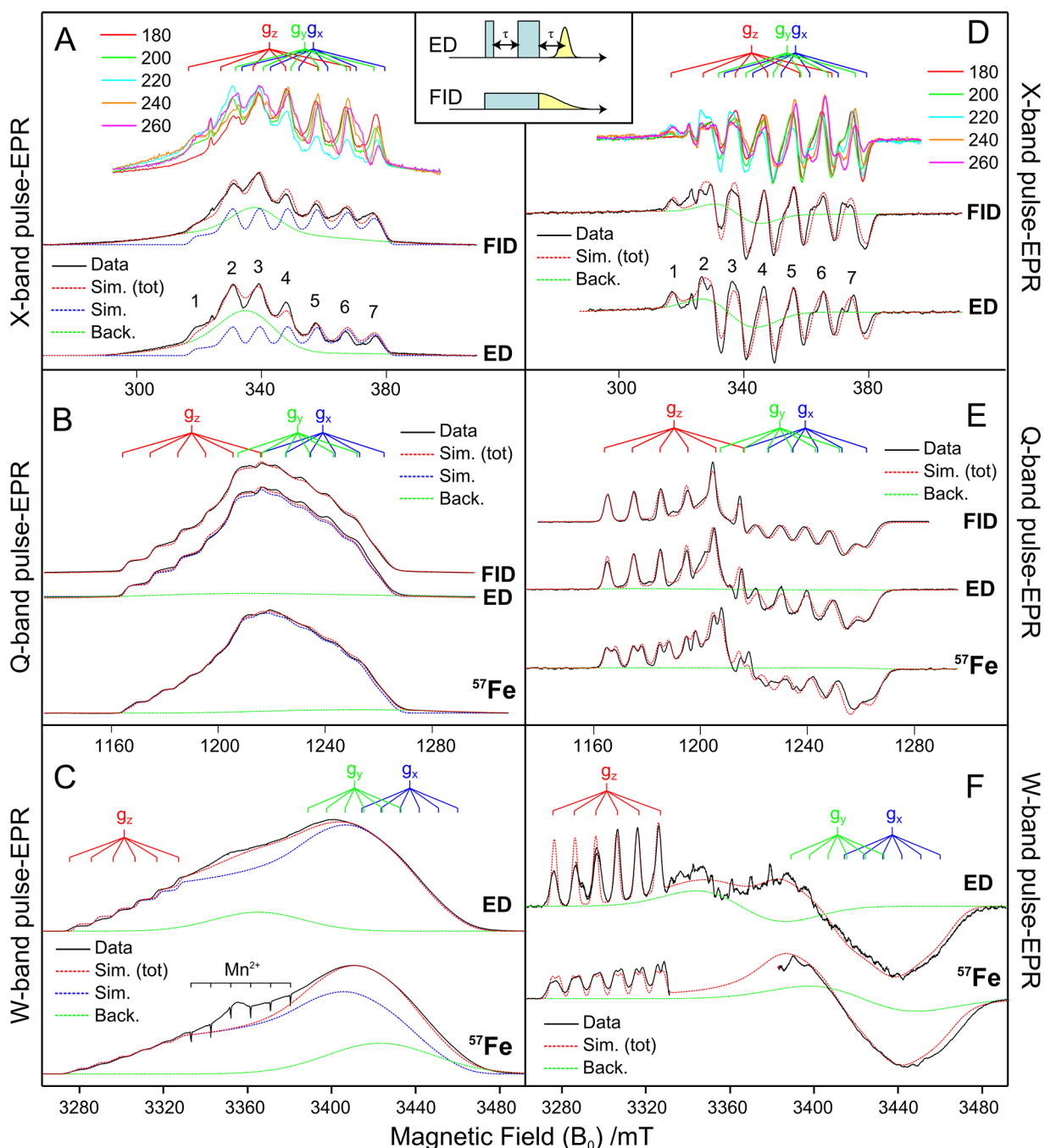
**Figure 3.** EPR spectra (black lines) and spin Hamiltonian simulations of the R2lox cofactor (red dashed lines, inclusive of background; blue dashed lines, exclusive of background; green dashed line, background). (A, D) Pulse X-band (9.77 GHz) EPR spectra of the $Mn^{III}/Fe^{III}$ metallocofactor observed in *Gk*R2loxI. (B, E) Corresponding pulse Q-band (33.9 GHz) EPR spectra.[23] (C, F) Corresponding pulse W-band (94.0 GHz) EPR spectra. Data on the left-hand side (LHS) represent the measured absorption spectra. Data on the right-hand side represent pseudomulated (CW-like) spectra shown on the LHS. Parameters for the simulation are given in Table 1. Experimental parameters are given in the Experimental Section and Supporting Information S1.

S2). Its EPR spectrum is centered about $g \approx 2$ with no additional signals observed at lower magnetic fields. It displays a simpler six-line structure at both X-band and Q-band frequencies but with larger average line spacings of 140 mT. This larger, apparent hyperfine interaction was confirmed by $^{55}Mn$-ENDOR (Figure 5). $^{57}Fe$ labeling of the cofactor led to further isotropic line broadening, confirming the signal arises from a spin-coupled Mn/Fe system (Figure 5). In addition to the metal-centered signal described above, a radical-like signal centered at $g \approx 2$ was also observed.

Spectral simulations demonstrate that the R2lox$_{Photo}$ signal differs from the precursor R2lox signal in terms of (i) its *g*-tensor, with a larger isotropic *g*-value ($g_{iso}$) and a smaller *g* anisotropy, (ii) its isotropic $^{55}Mn$ hyperfine coupling ($A_{iso}$), which is significantly larger (263 vs 354 MHz), (iii) the anisotropic component of its $^{55}Mn$ hyperfine tensor, which now takes the opposite sign, and (iv) its $^{57}Fe$ hyperfine tensor, which is approximately isotropic. Interestingly, it is noted that the photolyzed R2lox state displays similar EPR parameters as
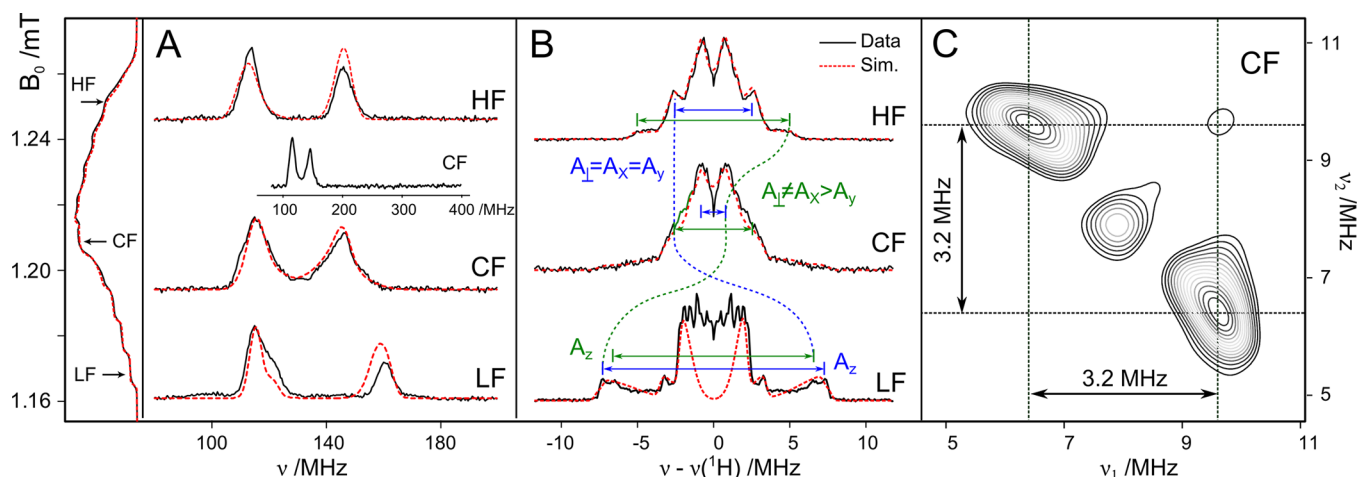
**Figure 4.** Q-band $^{55}$Mn-ENDOR (A), $^{1}$H-ENDOR (B), and $^{2}$H-HYSCORE (C) spectra of the R2lox cofactor at three field positions within the EPR absorption envelope (see Figure 3): low field (LF), 1169 mT; center field (CF), 1210 mT; high field (HF), 1251 mT. Black solid lines represent the experimental data; dashed red lines represent simultaneous simulation of the entire data set shown in Figures 2 and 3. $^{1}$H-ENDOR spectra were symmetrized about the respective $\nu(^{1}$H) Larmor frequency. Experimental parameters are given in the Experimental Section and Supporting Information S4.
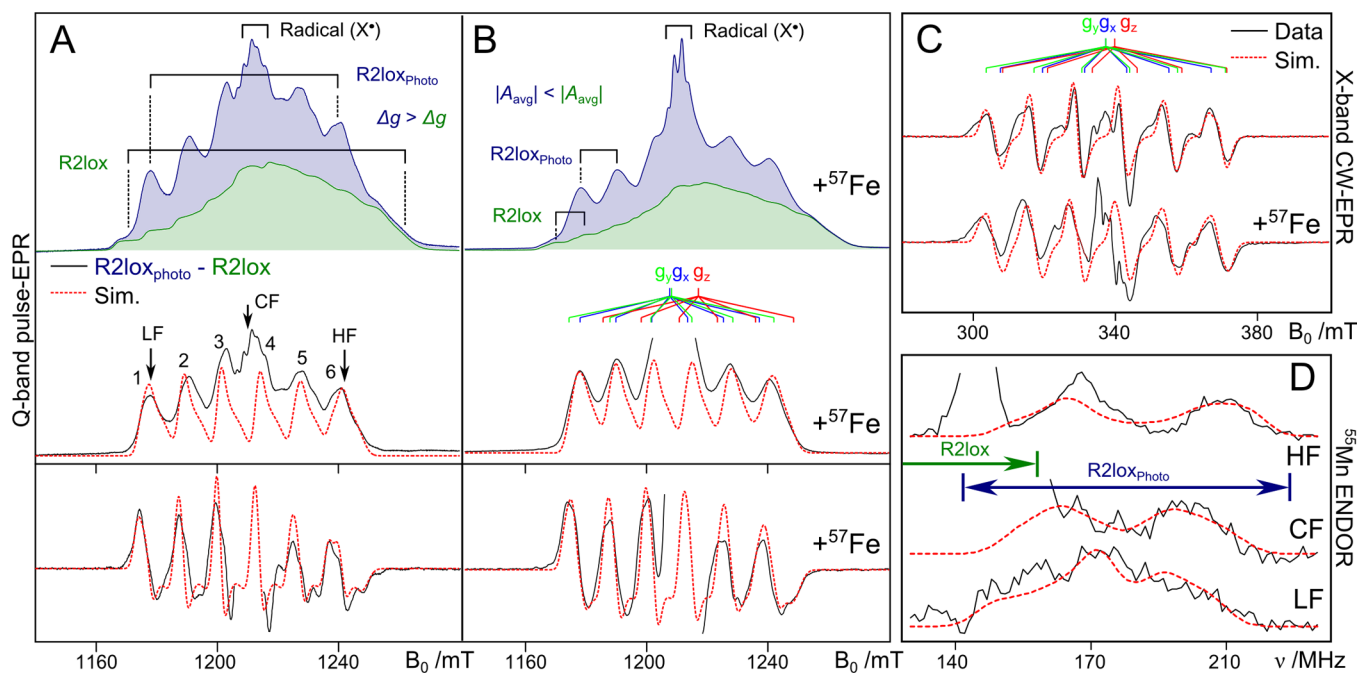


**Figure 5.** ESE-detected Q-band (33.9 GHz) (A and B), CW X-band (9.47 GHz) EPR (C), and Q-band $^{55}$Mn-ENDOR (D) spectra of the photolyzed Mn$^{III}$/Fe$^{III}$ R2lox sample reconstituted with natural abundance and $^{57}$Fe-enriched iron. Simulations are overlaid as red dashed traces; spin Hamiltonian parameters are given in Table 1. $^{55}$Mn-ENDOR were collected at three field positions within the EPR absorption envelope: low field (LF), 1169 mT; center field (CF), 1210 mT; high field (HF), 1251 mT. Experimental parameters are given in the Experimental Section and Supporting Information S2.

the Mn/Fe cofactor of R2c[5,6] (see Table 1, Supporting Information S2).

**3.4. Local EPR Parameters for the Mn and Fe Ions of the R2lox Metallocofactor.** The EPR parameters deduced from the above spectral simulations (Table 1) demonstrate that the local electronic structure of the Mn site in R2lox is fundamentally different from R2lox$_{photo}$. The $^{55}$Mn hyperfine parameters determined for R2lox require the Mn$^{III}$ ion of the cofactor to have a $^{5}$B$_1$ local electronic state, consistent with a tetragonally elongated metal site (Figure 6, Supporting Information S3). This is the same Mn site geometry seen in the X-ray crystal structure, confirming that the crystal structure

is a valid model for the solvated metallocofactor. In contrast, $^{55}$Mn hyperfine parameters determined for R2lox$_{Photo}$ require the Mn$^{III}$ ion of the cofactor to have a $^{5}$A$_1$ local electronic state as is seen for the Mn superoxide dismutase (Mn–SOD).[62,63] This change in local electronic structure should manifest in terms of an altered ligand geometry of the Mn$^{III}$ ion, with the Mn site now displaying structural compression along its unique axis (Figure 6, Supporting Information S3). In practice, such an assignment may be complicated by the influence of metal–ligand interactions of varying degrees of $\pi$ bonding. A tetragonally elongated and compressed Mn$^{III}$ site geometry

**Table 1. EPR Parameters Used To Simulate the R2lox and R2lox$_{Photo}$ Signals**

| | | | hyperfine/MHz | | | |
| | | | projected ($A_i$) | | intrinsic ($a_i$) | |
| | | g | Mn | Fe | Mn | Fe |
|---|---|---|---|---|---|---|
| R2lox | x | 1.953 | 257 | 62.5 | 270 | 32.0 |
| | y | 1.968 | 249 | 51.6 | 260 | 26.4 |
| | z | 2.034[a] | 282[a] | 93.9[a] | 127[a] | 29.2 |
| | iso | 1.985 | 263 | 69.3 | 219 | 29.2 |
| | aniso | 0.073 | 29.3 | 36.9 | −138 | 0 |
| R2lox$_{Photo}$ | x | 2.005 | 331 | | 248 | |
| | y | 2.004 | 379[a] | ≈60 | 284[a] | ≈26 |
| | z | 1.990[a] | 353 | | 264 | |
| | iso | 2.000 | 354 | ≈60 | 266 | ≈26 |
| | aniso | −0.015 | 36.8 | 0 | 27.6 | 0 |

[a]Indicates unique axis. Isotropic $g_{iso}$ and $A_{iso}$ values are the average of the individual values: $g_{iso} = (g_x + g_y + g_z)/3$ and $A_{iso}= (A_x + A_y + A_z)/3$. The anisotropy in the $g$ and $A_i$ values is expressed as the difference between the unique axis component and the average of the other two components. For calculation of the intrinsic hyperfine parameters see Supporting Information S3.
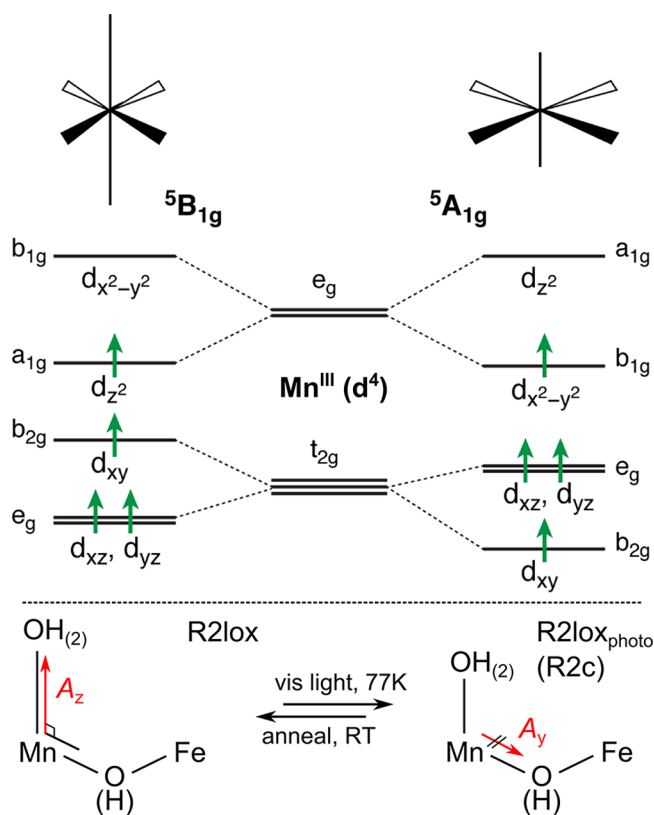


**Figure 6.** (Top) Idealized orbital splitting diagram for tetragonal elongation (left) and tetragonal compression (right) of a perfect octahedron, leading to electronic states $^5B_{1g}$ and $^5A_{1g}$, respectively, in the case of a high-spin Mn$^{III}$ ion. (Bottom) Proposed local site geometry of the Mn$^{III}$ ion of the Mn/Fe cofactor of R2lox and R2lox$_{Photo}$. The R2lox cofactor shows a tetragonal elongation of bonds perpendicular to the $\mu$-O(H) bridge, whereas the R2lox$_{Photo}$/R2c cofactor shows a tetragonal compression parallel to the $\mu$-O(H) bridge.

have both been observed in synthetic $\mu$-oxo, bis-$\mu$-carboxylato-bridged Mn$^{III}$/Mn$^{III}$ dimer complexes. In structures which

contain a tetragonal elongation of the Mn$^{III}$ ion, the unique (Jahn−Teller) axis lies perpendicular to the Mn−$\mu$-oxo bridge vector,[64,65] as seen for the R2lox cofactor. In contrast, in structures which contain a tetragonally compressed Mn$^{III}$ ion, the unique axis lies in the direction of the Mn−$\mu$-oxo bridge vector.[66,67] The compression is inferred from the short nitrogen-donor atom distance trans to the Mn−$\mu$-oxo bond, which has the same distance as the nitrogen donors being cis to that bond. This is a strong indication of a compressed geometry as the trans donor distance should be about 0.1−0.2 Å longer due to the trans influence of the oxo donor, as observed in related iron dimers.[68−70] Thus, photolysis likely rotates the unique axis of the cofactor.

**3.5. Development of a Structural Model: A $\mu$-OH-Bridged Cofactor with a Terminal Water Ligand.** The protonation state of the R2lox cofactor was assessed using two techniques, $^1$H-Davies ENDOR and $^2$H-ESEEM/HYSCORE. Figure 4B shows the $^1$H-ENDOR spectrum of R2lox measured at the low-, center-, and high-field edges of the absorption envelope. These spectra represent the superposition of multiple $^1$H signals, which appear symmetrically centered about the $^1$H nuclear Larmor frequency [$\nu(^1H)$ = 51.9 MHz at 1.22 T] with their width/splitting defined by the hyperfine coupling.

The coupling between a $^1$H nucleus and an electron spin is usually dominantly a through space, dipole−dipole interaction ($A_{dip}$). Thus, the magnitude of the hyperfine interaction informs on the distance between the proton and the metal ions of the cofactor. The two largest hyperfine couplings observed in the $^1$H-ENDOR spectra are both ≈7 MHz, consistent with two protons 2.5 Å away from the Mn$^{III}$ ion, i.e., the two protons of a water ligand. The magnetic field dependence of the ENDOR profile supports this assignment and demonstrates that the two water protons are inequivalent: one proton signal shows axial symmetry, while the second displays rhombic symmetry (Supporting Information S4). This inequivalence may be a consequence of the protein pocket. One of the water protons most likely hydrogen bonds to Glu202, locating it proximal to the Fe$^{III}$ site, whereas the second proton would point away from the Fe$^{III}$ site (Figure 1C). The remaining $^1$H-ENDOR envelope represents protein residue protons in the immediate vicinity of the metallocofactor (<5 MHz, <5 Å).

A third, larger hyperfine coupling was observed by deuterating the cofactor and detection via $^2$H-ESEEM/HYSCORE (Figure 4C). The $^2$H-HYSCORE spectrum measured in the center of the EPR spectrum reveals a doublet signal in the (+,+) quadrant centered around the diagonal at the $^2$H Larmor frequency ($\nu(^2H)$ = 7.97 MHz at 1.22 T), split by a hyperfine coupling of ≈3 MHz. It is noted that to directly compare $^2$H and $^1$H hyperfine couplings the $^2$H value should be multiplied by 6.51 (owing to the difference in their intrinsic magnetic moments), yielding an effective $^1$H coupling of ≈21 MHz. This very large proton coupling can be assigned to a $\mu$-OH bridge proton. Its magnitude comes about because the bridging oxygen to which it is bound carries significant spin density as it mediates the metal−metal exchange interaction (see Supporting Information S4).

**3.6. Possible Mismetalation under Aerobic Conditions: Exchange of the Metal Sites?** The X-ray structure of R2lox identifies a histidine residue coordinated to each metal ion (Figure 1C). In the coupled spin system, these two histidines should give rise to two inequivalent $^{14}$N signals and thus provide a novel means to test if mismetalated (Fe/Mn)
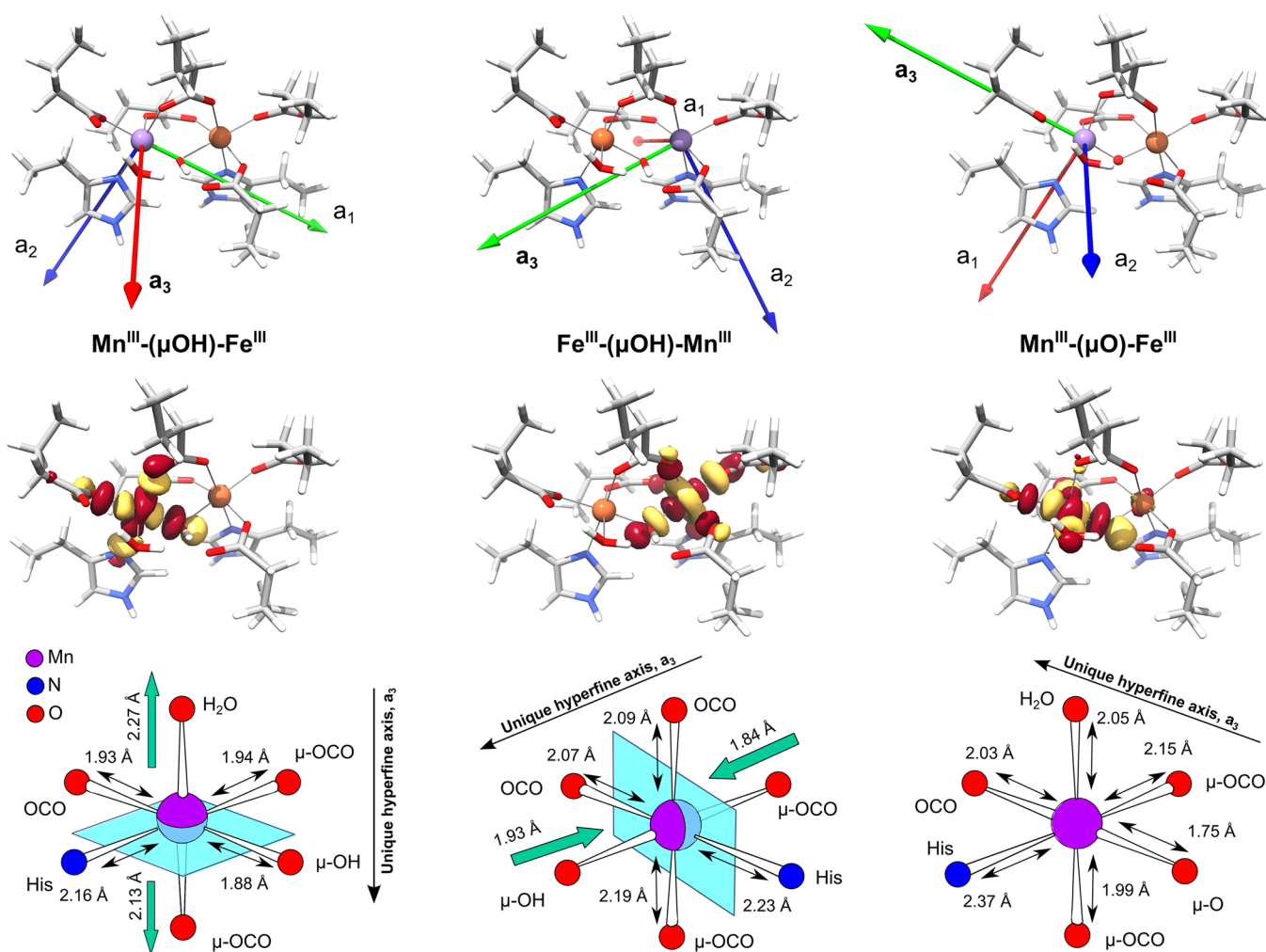
**Figure 7.** (Top) Calculated onsite $^{55}$Mn hyperfine tensor orientations for the three model R2lox cofactors, (middle) corresponding LUMO for each structure, and (bottom) local site geometry of the Mn$^{III}$ ion. The three structures differ in terms of their electronic structure, with the character of the Mn-centered LUMO changing from predominantly d($x^2 - y^2$) for the oxidized Mn/Fe cofactor to predominantly d($z^2$) for the mismetalated Fe/Mn cofactor. The oxo-bridged species serves as a model for the photolyzed state; it forms an intermediate state that more closely resembles the mismetalated cofactor. Arrows showing the hyperfine tensor axes are colored: green, blue, red in order of decreasing magnitude.

**Table 2. Calculated Onsite $^{55}$Mn and $^{57}$Fe Hyperfine Tensors for the Three Model R2lox Cofactors ($\mu$-hydroxo bridged, mismetalated, $\mu$-oxo bridged); Comparison to Experimental Values**

| | | calculated onsite metal nuclei hyperfine tensors $|a_i|$/MHz | | | | | | | | | |
| | | Mn$^{III}$ | | | | | Fe$^{III}$ | | | | |
| | $J$/cm$^{-1}$ | $a_1$ | $a_2$ | $a_3$ | $a_{iso}$ | $a_{aniso}$ | $a_1$ | $a_2$ | $a_3$ | $a_{iso}$ | $a_{aniso}$ |
|---|---|---|---|---|---|---|---|---|---|---|---|
| Mn$-(\mu-$OH$)-$Fe | −16.8 | 274 | 207 | 129 | 203 | −112 | 25.2 | 26.0 | 26.6 | 25.9 | 1.1 |
| Fe$-(\mu-$OH$)-$Mn | −16.9 | 194 | 202 | 326 | 240 | 128 | 26.2 | 26.4 | 27.0 | 26.6 | 0.7 |
| Mn$-(\mu$-O$)-$Fe | −82.7 | 124 | 199 | 278 | 201 | 116 | 21.4 | 22.1 | 24.1 | 22.5 | 2.3 |
| exp. | −1.8 to −8.0[a] | 270 | 260 | 127 | 219 | −138 | 32.0 | 26.4 | 29.2 | 29.2 | 0 |
| exp. (photo) | >20 | 248 | 264 | 284 | 266 | 27.6 | 26 | 26 | 26 | 26 | 0 |

[a]Assuming an onsite d(Mn$^{III}$) = −1.1 to −5.0 cm$^{-1}$; $\rho$(Fe) = [$\rho_1$ $\rho_2$ $\rho_3$] = [1.95 1.95 3.21]; $\rho$(Mn) = [$\rho_1$ $\rho_2$ $\rho_3$] = [−0.95 −0.95 −2.21]

centers exist under solution loading conditions. The $^{14}$N His105 signal of the Mn$^{III}$ ion was observed by X-band ESEEM. Its hyperfine and quadrupole couplings are typical of synthetic mixed-valent Mn$^{III}$/Mn$^{IV}$ complexes, such as the superoxidized state of the Mn−catalase[35] (Supporting Information S5). Similarly, the $^{14}$N His205 signal of the Fe$^{III}$ ion was observed by W-band ESEEM, with hyperfine couplings now similar to those measured for Fe$^{III}$/Fe$^{IV}$ complexes[71] (Supporting Information S5). In addition to the two anticipated nitrogen

signals, a third $^{14}$N signal was observed using Q-band ESEEM but only when measuring ESEEM between the low-field edge and the center field of the EPR spectrum (Supporting Information S5). This signal is taken as evidence for a second underlying cofactor signal, representing ∼5% of centers. DFT calculations shown in the next section support the assignment of this second species to a mismetalated Fe$^{III}$/Mn$^{III}$ cofactor.

**3.7. DFT Calculations.** Using the spectroscopic data above, DFT models were developed for the R2lox and R2lox$_{Photo}$

cofactor. Three basic structures were examined, representing optimized geometries of the crystal structure assuming a III/III oxidation state for both ions.[23] Two features were varied: the metal identity of sites 1 and 2 and the protonation of the bridging ligand (oxo/hydroxo). A set of three DFT models described below is sufficient to explain all EPR observations (Figure 7).

*3.7.1. A $Mn^{III}-(\mu-OH)-Fe^{III}$ Cofactor.* Mn is bound at site 1 with its ligand sphere completed by a water ligand, and Fe is bound at site 2 (Figure 7). The two metal sites are linked by a $\mu$-OH bridge. This structure represents the aerobically prepared R2lox cofactor, reproducing all crystallographic and spectroscopic constraints, namely, (i) the metal−metal distance: 3.55 (exp) vs 3.48 Å (DFT), (ii) the metal−OH distance: 2.12 (exp) vs 2.08 Å (DFT), (iii) the metal−bridge−metal angle: 107° (exp) vs 126° (DFT), (iv) the local site geometry of the Mn ion, with elongation along the Mn−OH$_2$ axis, perpendicular to the $Mn^{III}-(\mu-OH)-Fe^{III}$ plane (Figure 7), (v) the local site geometry of the Fe ion, which is approximately spherically symmetric, (vi) the small exchange coupling, inferred from EPR simulations (see Supporting Information S3), typical of $\mu$-OH dimers,[38,39] and (vii) the complete set of EPR observables described above (Table 2 and Supporting Information S6). It is noted that the Mn$^{III}$ ion displays a local high-spin d$(xy)^1$d-$(xz)^1$d$(yz)^1$d$(z^2)^1$ electronic configuration (a "$^5B_1$"-like ground state). The HOMO, of Mn d$(z^2)$ origin, is oriented along the Mn−OH$_2$ axis. Its strongly antibonding metal−ligand $\sigma^*$ character leads to the observed elongation of the corresponding bonds. Accordingly, the LUMO of the cofactor is of Mn d$(x^2-y^2)$ origin (Figure 7). Since this orbital, which corresponds to the $\sigma^*$ interaction of the Mn ion with the equatorial ligands, remains unoccupied, the equatorial bonds such as Mn−N are exceptionally short in this structure.

*3.7.2. A $Fe^{III}-(\mu-OH)-Mn^{III}$ Cofactor.* Fe is bound at site 1 with its ligand sphere completed by a water ligand, while Mn is bound at site 2 (Figure 7). This mismetalated cofactor displays a $^{14}$N hyperfine coupling of approximately the same magnitude for the minority species described in section 3.6, assigned to the $^{14}$N His205 of what is now the Mn$^{III}$ ion. Compared with the R2lox model discussed above, a change in the local electronic configuration of the Mn ion is observed, with the frontier orbitals swapping metal character, i.e., the HOMO is now of Mn d$(x^2-y^2)$ origin and the LUMO is the Mn d$(z^2)$, oriented along the Mn−OH axis (Figure 7). In line with this change in electronic configuration, the local geometry of Mn$^{III}$ is tetragonally compressed, with the unique, short axis lying along the Mn−OH vector. It is also noted that this structure displays the same ground electronic state ($S = 1/2$), the same spin density distribution, and a similar $^{55}$Mn-hyperfine coupling, so it should yield a similar EPR spectrum of approximately the same spectral width. However, owing to the change in the electronic configuration of the Mn$^{III}$ ion (a local "$^5A_1$"-like ground state as opposed to a local $^5B_1$-like state seen for the oxidized R2lox) its g-tensor is likely altered, as also inferred from experiment. This mismetalated structure is predicted to be of slightly higher energy compared to the R2lox model described above (+2.2 kcal mol$^{-1}$) and as such is not thermodynamically favored, consistent with its apparent small population in solution.[23,72]

*3.7.3. A $Mn^{III}-(\mu-O)-Fe^{III}$ Cofactor.* As in the first model, Mn is bound at site 1 with its ligand sphere completed by a water ligand and Fe is bound at site 2. However, the two metal sites are now linked by a $\mu$-oxo bridge. This bridging motif

leads to a larger calculated exchange interaction between the two metal ions, as inferred from EPR simulations (see Supporting Information S3).

This structure represents a good candidate for the photolyzed state of the R2lox cofactor and appears to display many of the characteristics associated with the Mn$^{III}$/Fe$^{III}$ cofactor of R2c. Unlike the Mn$^{III}$ ion of the R2lox and mismetalated cofactor, DFT calculations suggest that the photolyzed state represents a mixed state from a structural as well as an electronic point of view. Specifically, both the HOMO and the LUMO have mixed d$(z^2)$ and d$(x^2-y^2)$ Mn character, and analysis of the metal−ligand interactions is complicated by the presence of a $\pi^*$ interaction in the HOMO between the oxo bridge and the Mn ion (Figure 7, Supporting Information S6). Nevertheless, it is clear from the optimized geometry that the Jahn−Teller axis of the tetragonally elongated R2lox model is lost in the photolyzed state. It is less clear from inspection of the structure alone whether there is a simple reorientation of the Jahn−Teller axis along the Mn−His vector (in which case this should be assigned as the local z axis with respect to Mn orbital character) or whether the elongation of the Mn−His and Mn−OCO bonds is a result of the significant d$(x^2-y^2)$ metal−ligand $\sigma^*$ character in the HOMO. The presence of tetragonal compression (along the Mn−oxo bond) in the latter case would be masked to some extent by the simultaneous presence of the Mn−oxo $\pi^*$ interaction in the HOMO (Figure S6, Supporting Information). The picture is greatly clarified when the calculated EPR parameters are considered: the computed $^{55}$Mn hyperfine tensors more closely resemble those seen for the mismetalated cofactor (Table 2), allowing us to assign an effective $^5A_1$-like local ground state to the Mn$^{III}$ ion of the model for the photolyzed cofactor. This change in the local electronic structure implies (as described in section 3.6) that the unique axis of the system rotates into the plane of the Mn−$(\mu$-O)−Fe bridge, lying along the Mn−$(\mu$-O) bond (Figure 7, Table 2, Supporting Information S6). This structure is thus fully consistent with EPR data on the photolyzed state. It is proposed that the photolyzed state represents the photo-induced migration of the $\mu$-OH bridge proton, as has been previously observed for the heterobimetallic metal cofactors of the [NiFe] hydrogenases,[73,74] and may be related to light-induced changes seen in myoglobin.[75] In R2lox, it is hypothesized that the displaced proton may migrate to a nearby protein residue. The noncoordinating oxygen of Glu202, which is only 2.7 Å away from the bridging $\mu$-OH, could potentially fill this role. This residue bridges the two metals in the reduced state, rotating out of this bridging position upon cofactor activation (Figure 1C and 1D).

**3.8. Comparison of R2c and R2lox.** The photolyzed R2lox state appears to share many of the same EPR properties observed for the Mn$^{III}$/Fe$^{III}$ state of the cofactor of R2c,[5,6] as described above. This correspondence suggests that the photolyzed state of R2lox represents an electronic model for R2c, especially in terms of the Mn$^{III}$ site. The comparison implies that the Mn$^{III}$/Fe$^{III}$ state of R2c most likely contains a Mn$^{III}$ ion with a tetragonally compressed ligand field, such that the unique axis of the Mn$^{III}$ ion is aligned along the Mn−$\mu$-oxo bridge bond vector, not along the Mn−OH$_2$ bond vector as seen for the R2lox cofactor. Since the reorientation of the unique axis of the Mn$^{III}$ ion is driven by bridge deprotonation, it is postulated that the R2c cofactor contains at least one $\mu$-oxo bridge in the Mn$^{III}$/Fe$^{III}$ state. We note that a $\mu$-oxo/$\mu$-hydroxo bridged cofactor with a terminal water ligand was favored as the

most likely R2c cofactor in a recent NRVS/MCD study,[76] in line with our results.

The NRVS/MCD study thus assigned the total charge of the R2c cofactor to −1 in both its $Mn^{IV}/Fe^{III}$ and its $Mn^{III}/Fe^{III}$ oxidation states.[76] The same negatively charged $Mn^{IV}/Fe^{III}$ active cofactor structure was, in an earlier DFT study, shown to have the correct redox properties to replace the tyrosyl radical of class Ia R2.[77] A total charge of −1 is also found here for the R2lox$_{Photo}$ cofactor, in line with earlier DFT studies on R2lox.[23] Thus, from an electronic perspective, the R2lox and R2lox$_{Photo}$ cofactors and by extension the R2lox and R2c cofactors primarily differ in terms of the local electronic state of the $Mn^{III}$ ion. This property alone must dictate the different redox properties of the two cofactors and their divergent catalytic function.

## 4. CONCLUSION

The analysis presented above suggests the Mn/Fe cofactor of R2lox and that of its homologue R2c represent similar but not identical electronic motifs. This electronic flexibility must in part explain the chemical versatility of the Mn/Fe cofactor, directing its chemistry toward either 1e$^-$/hole transfer and storage (at the Mn site) in the case of R2c or 2e$^-$ oxidation of a potential substrate occupying the open (water) coordination site in the case of R2lox. Chemical versatility is achieved by tuning the local electronic structure and thus redox properties of the Mn ion itself. In R2lox, the $\mu$-hydroxo/$\mu$-carboxylato bridging network stabilizes a tetragonally elongated $Mn^{III}$ ion with the Jahn−Teller axis located perpendicular to the Mn−$\mu$-hydroxo bond, whereas in R2c, a $\mu$-oxo/$\mu$-hydroxo bridging network stabilizes a tetragonally compressed $Mn^{III}$ ion with the unique axis located parallel to the Mn−oxo bond. Both cofactors have a terminal water bound at the $Mn^{III}$ site. As seen in Figure 7, the electronic structure of the cofactor interchanges between a local $^5A_1$-like ground state with a LUMO of predominantly $d(z^2)$ character to a $^5B_1$-like ground state with a LUMO of predominantly $d(x^2-y^2)$ character. This interchange leads to a reorientation of the unoccupied orbital such that it does not coincide with the open (water) coordination site in the R2lox structure, favoring 2e$^-$ vs 1e$^-$ redox chemistry.

## ASSOCIATED CONTENT

### Ⓢ Supporting Information

Multifrequency CW and pulse EPR data of the Mn/Fe cofactor of R2lox and microwave nutation curves; optical absorption data of the activated R2lox and time course of the induction of the photolyzed state (R2lox$_{Photo}$); estimates of the metal−metal exchange and fine structure parameters of the R2lox Mn/Fe cofactor (comparison to literature R2c data), Q-band $^1H/^2H$ ESEEM/ENDOR data of the R2lox cofactor; $^{14}N$ ESEEM of the R2lox cofactor, evidence for a mismetalated cofactor; tabulated DFT parameters; references. This material is available free of charge via the Internet at http://pubs.acs.org.

## AUTHOR INFORMATION

### Corresponding Author

E-mail: nicholas.cox@cec.mpg.de

### Present Addresses

H. S. Shafaat: Department of Chemistry and Biochemistry, The Ohio State University, Columbus, OH 43210, United States.
A. Popović-Bijelić: Faculty of Physical Chemistry, University of Belgrade, 11158, Belgrade, Serbia.

## REFERENCES

(1) Lubitz, W.; Ogata, H.; Rüdiger, O.; Reijerse, E. *Chem. Rev.* **2014**, *114*, 4081−4148.

(2) Michel, H.; Behr, J.; Harrenga, A.; Kannt, A. *Annu. Rev. Biophys. Biomed.* **1998**, *27*, 329−356.

(3) Fridovich, I. *Annu. Rev. Biochem.* **1975**, *44*, 147−159.

(4) Schenk, G.; Boutchard, C. L.; Carrington, L. E.; Noble, C. J.; Moubaraki, B.; Murray, K. S.; de Jersey, J.; Hanson, G. R.; Hamilton, S. *J. Biol. Chem.* **2001**, *276*, 19084−19088.

(5) Jiang, W.; Yun, D.; Saleh, L.; Barr, E. W.; Xing, G.; Hoffart, L. M.; Maslak, M.-A.; Krebs, C.; Bollinger, J. M., Jr. *Science* **2007**, *316*, 1188−1191.

(6) Voevodskaya, N.; Lendzian, F.; Ehrenberg, A.; Gräslund, A. *FEBS Lett.* **2007**, *581*, 3351−3355.

(7) Zocher, G.; Winkler, R.; Hertweck, C.; Schulz, G. E. *J. Mol. Biol.* **2007**, *373*, 65−74.

(8) Choi, Y. S.; Zhang, H.; Brunzelle, J. S.; Nair, S. K.; Zhao, H. *Proc. Natl. Acad. Sci. U.S.A.* **2008**, *105*, 6858−6863.

(9) Krebs, C.; Matthews, M. L.; Jiang, W.; Bollinger, J. M., Jr. *Biochemistry* **2007**, *46*, 10413−10418.

(10) Stubbe, J.; Nocera, D. G.; Yee, C. S.; Chang, M. C. Y. *Chem. Rev.* **2003**, *103*, 2167−2201.

(11) Nordlund, P.; Reichard, P. *Annu. Rev. Biochem.* **2006**, *75*, 681−706.

(12) Bollinger, J. M., Jr.; Jiang, W.; Green, M. T.; Krebs, C. *Curr. Opin. Struc. Biol.* **2008**, *18*, 650−657.

(13) Nordlund, P.; Sjöberg, B.; Eklund, H. *Nature* **1990**, *345*, 593−598.

(14) Uhlin, U.; Eklund, H. *Nature* **1994**, *370*, 533−539.

(15) Sjöberg, B. In *Metal Sites in Proteins and Models*; Allen, H., Hill, O., Sadler, P. J., Thomson, A. J., Eds.; Springer: Berlin, 1997; Vol. 88, pp 139−183.

(16) Cox, N.; Ogata, H.; Stolle, P.; Reijerse, E.; Auling, G.; Lubitz, W. *J. Am. Chem. Soc.* **2010**, *132*, 11197−11213.

(17) Cotruvo, J. A., Jr.; Stubbe, J. *Biochemistry* **2010**, *49*, 1297−1309.

(18) Cotruvo, J. A., Jr.; Stubbe, J. *Annu. Rev. Biochem.* **2011**, *80*, 733−767.

(19) Cotruvo, J. A., Jr.; Stich, T. A.; Britt, R. D.; Stubbe, J. *J. Am. Chem. Soc.* **2013**, *135*, 4027−4039.

(20) Högbom, M.; Stenmark, P.; Voevodskaya, N.; McClarty, G.; Gräslund, A.; Nordlund, P. *Science* **2004**, *305*, 245−248.

(21) Dassama, L. M. K.; Krebs, C.; Bollinger, J. M., Jr.; Rosenzweig, A. C.; Boal, A. K. *Biochemistry* **2013**, *52*, 6424−6436.

(22) Andersson, C. S.; Högbom, M. *Proc. Natl. Acad. Sci. U.S.A.* **2009**, *106*, 5633−5638.

(23) Griese, J. J.; Roos, K.; Cox, N.; Shafaat, H. S.; Branca, R. M. M.; Lehtiö, J.; Gräslund, A.; Lubitz, W.; Siegbahn, P. E. M.; Högbom, M. *Proc. Natl. Acad. Sci. U.S.A.* **2013**, *110*, 17189−17194.

(24) Roos, K.; Siegbahn, P. E. M. *J. Biol. Inorg. Chem.* **2012**, *17*, 363−373.

(25) Andersson, C. S.; Öhrström, M.; Popović-Bijelić, A.; Gräslund, A.; Stenmark, P.; Högbom, M. *J. Am. Chem. Soc.* **2012**, *134*, 123−125.

(26) Dassama, L. M.; Boal, A. K.; Krebs, C.; Rosenzweig, A. C.; Bollinger, J. M., Jr. *J. Am. Chem. Soc.* **2012**, *134*, 2520−2523.

(27) Sigfridsson, K. G. V.; Chernev, P.; Leidel, N.; Popović-Bijelić, A.; Gräslund, A.; Haumann, M. *J. Biol. Chem.* **2013**, *288*, 9648–9661.

(28) Eriksson, M.; Jordan, A.; Eklund, H. *Biochemistry* **1998**, *37*, 13359–13369.

(29) Logan, D. T.; Su, X. D.; Aberg, A.; Regnström, K.; Hajdu, J.; Eklund, H.; Nordlund, P. *Structure* **1996**, *4*, 1053–1064.

(30) Younker, J. M.; Krest, C. M.; Jiang, W.; Krebs, C.; Bollinger, J. M., Jr.; Green, M. T. *J. Am. Chem. Soc.* **2008**, *130*, 15022–15027.

(31) Britt, R. D.; Campbell, K. A.; Peloquin, J. M.; Gilchrist, M. L.; Aznar, C. P.; Dicus, M. M.; Robblee, J.; Messinger, J. *Biochim. Biophys. Acta* **2004**, *1655*, 158–171.

(32) Cox, N.; Rapatskiy, L.; Su, J.-H.; Pantazis, D. A.; Sugiura, M.; Kulik, L.; Dorlet, P.; Rutherford, A. W.; Neese, F.; Boussac, A.; Lubitz, W.; Messinger, J. *J. Am. Chem. Soc.* **2011**, *133*, 3635–3648.

(33) McConnell, I. L.; Grigoryants, V. M.; Scholes, C. P.; Myers, W. K.; Chen, P.-Y.; Whittaker, J. W.; Brudvig, G. W. *J. Am. Chem. Soc.* **2011**, *134*, 1504–1512.

(34) Rapatskiy, L.; Cox, N.; Savitsky, A.; Ames, W. M.; Sander, J.; Nowaczyk, M. M.; Rögner, M.; Boussac, A.; Neese, F.; Messinger, J.; Lubitz, W. *J. Am. Chem. Soc.* **2012**, *134*, 16619–16634.

(35) Stich, T. A.; Whittaker, J. W.; Britt, R. D. *J. Phys. Chem. B* **2010**, *114*, 14178–14188.

(36) Raitsimring, A. M.; Astashkin, A. V.; Baute, D.; Goldfarb, D.; Caravan, P. *J. Phys. Chem. A* **2004**, *108*, 7318–7323.

(37) Goldfarb, D.; Lipkin, Y.; Potapov, A.; Gorodetsky, Y.; Epel, B.; Raitsimring, A. M.; Radoul, M.; Kaminker, I. *J. Magn. Reson.* **2008**, *194*, 8–15.

(38) Bossek, U.; Weyhermüller, T.; Wieghardt, K.; Bonvoisin, J.; Girerd, J. J. *J. Chem. Soc., Chem. Commun.* **1989**, 633–636.

(39) Cox, N.; Ames, W.; Epel, B.; Kulik, L. V.; Rapatskiy, L.; Neese, F.; Messinger, J.; Wieghardt, K.; Lubitz, W. *Inorg. Chem.* **2011**, *50*, 8238–8251.

(40) Reijerse, E.; Lendzian, F.; Isaacson, R.; Lubitz, W. *J. Magn. Reson.* **2012**, *214*, 237–243.

(41) Stoll, S.; Schweiger, A. *J. Magn. Reson.* **2006**, *178*, 42–55.

(42) Stoll, S.; Britt, R. D. *Phys. Chem. Chem. Phys.* **2009**, *11*, 6614–6625.

(43) Noodleman, L. *J. Chem. Phys.* **1981**, *74*, 5737–5743.

(44) Yamaguchi, K.; Tsunekawa, T.; Toyoda, Y.; Fueno, T. *Chem. Phys. Lett.* **1988**, *143*, 371–376.

(45) Neese, F. *Coordin. Chem. Rev.* **2009**, *253*, 526–563.

(46) Sinnecker, S.; Neese, F.; Noodleman, L.; Lubitz, W. *J. Am. Chem. Soc.* **2004**, *126*, 2613–2622.

(47) Neese, F. *WIREs Comput. Mol. Sci.* **2012**, *2*, 73–78.

(48) Staroverov, V. N.; Scuseria, G. E.; Tao, J.; Perdew, J. P. *J. Chem. Phys.* **2003**, *119*, 12129–12137.

(49) Orio, M.; Pantazis, D. A.; Petrenko, T.; Neese, F. *Inorg. Chem.* **2009**, *48*, 7251–7260.

(50) Neese, F.; Ames, W.; Christian, G.; Kampa, M.; Liakos, D. G.; Pantazis, D. A.; Roemelt, M.; Surawatanawong, P.; Ye, S. F. *Adv. Inorg. Chem.* **2010**, *62*, 301–349.

(51) Ames, W.; Pantazis, D. A.; Krewald, V.; Cox, N.; Messinger, J.; Lubitz, W.; Neese, F. *J. Am. Chem. Soc.* **2011**, *133*, 19743–19757.

(52) Pantazis, D. A.; Ames, W.; Cox, N.; Lubitz, W.; Neese, F. *Angew. Chem., Int. Ed.* **2012**, *51*, 9935–9940.

(53) Krewald, V.; Neese, F.; Pantazis, D. A. *J. Am. Chem. Soc.* **2013**, *135*, 5726–5739.

(54) Van Lenthe, E.; Baerends, E. J.; Snijders, J. G. *J. Chem. Phys.* **1993**, *99*, 4597–4610.

(55) Van Lenthe, E.; Baerends, E. J.; Snijders, J. G. *J. Chem. Phys.* **1994**, *101*, 9783–9792.

(56) Van Wüllen, C. *J. Chem. Phys.* **1998**, *109*, 392–399.

(57) Pantazis, D. A.; Chen, X. Y.; Landis, C. R.; Neese, F. *J. Chem. Theory Comput.* **2008**, *4*, 908–919.

(58) Weigend, F. *Phys. Chem. Chem. Phys.* **2006**, *8*, 1057–1065.

(59) Neese, F. *Inorg. Chim. Acta* **2002**, *337C*, 181–192.

(60) Anderlund, M. F.; Högblom, J.; Shi, W.; Huang, P.; Eriksson, L.; Weihe, H.; Styring, S.; Åkermark, B.; Lomoth, R.; Magnuson, A. *Eur. J. Inorg. Chem.* **2006**, 5033–5047.

(61) Kurtz, D. M. *Chem. Rev.* **1990**, *90*, 585–606.

(62) Whittaker, J. W.; Whittaker, M. M. *J. Am. Chem. Soc.* **1991**, *113*, 5528–5540.

(63) Campbell, K. A.; Force, D. A.; Nixon, P. J.; Dole, F.; Diner, B. A.; Britt, R. D. *J. Am. Chem. Soc.* **2000**, *122*, 3754–3761.

(64) Ménage, S.; Girerd, J.-J.; Gleizes, A. *J. Chem. Soc., Chem. Commun.* **1988**, 431–432.

(65) Wu, F. J.; Kurtz, D. M.; Hagen, K. S.; Nyman, P. D.; Debrunner, P. G.; Vankai, V. A. *Inorg. Chem.* **1990**, *29*, 5174–5183.

(66) Wieghardt, K.; Bossek, U.; Ventur, D.; Weiss, J. *J. Chem. Soc., Chem. Commun.* **1985**, 347–349.

(67) Sheats, J. E.; Czernuszewicz, R. S.; Dismukes, G. C.; Rheingold, A. L.; Petrouleas, V.; Stubbe, J.; Armstrong, W. H.; Beer, R. H.; Lippard, S. J. *J. Am. Chem. Soc.* **1987**, *109*, 1435–1444.

(68) Wieghardt, K.; Pohl, K.; Gebert, W. *Angew. Chem., Int. Ed.* **1983**, *22*, 727.

(69) Armstrong, W. H.; Lippard, S. J. *J. Am. Chem. Soc.* **1983**, *105*, 4837–4838.

(70) Armstrong, W. H.; Lippard, S. J. *J. Am. Chem. Soc.* **1984**, *106*, 4632–4633.

(71) Burdi, D.; Sturgeon, B. E.; Tong, W. H.; Stubbe, J.; Hoffman, B. M. *J. Am. Chem. Soc.* **1996**, *118*, 281–282.

(72) Roos, K.; Siegbahn, P. E. M. *J. Biol. Inorg. Chem.* **2011**, *16*, 553–565.

(73) Kampa, M.; Pandelia, M. E.; Lubitz, W.; van Gastel, M.; Neese, F. *J. Am. Chem. Soc.* **2013**, *135*, 3915–3925.

(74) Pandelia, M. E.; Ogata, H.; Currell, L. J.; Flores, M.; Lubitz, W. *J. Biol. Inorg. Chem.* **2009**, *14*, 1227–1241.

(75) Nilsson, K.; Hersleth, H.-P.; Rod, T. H.; Andersson, K. K.; Ryde, U. *Biophys. J.* **2004**, *87*, 3437–3447.

(76) Kwak, Y.; Jiang, W.; Dassama, L. M. K.; Park, K.; Bell, C. B.; Liu, L. V.; Wong, S. D.; Saito, M.; Kobayashi, Y.; Kitao, S.; Seto, M.; Yoda, Y.; Alp, E. E.; Zhao, J.; Bollinger, J. M., Jr.; Krebs, C.; Solomon, E. I. *J. Am. Chem. Soc.* **2013**, *135*, 17573–17584.

(77) Roos, K.; Siegbahn, P. E. M. *Biochemistry* **2009**, *48*, 1878–1887.